Application of Fano resonance effects in optical antennas formed by regular clusters of nanospheres

S. D. Emami · M. R. K. Soltanian · A. Attaran · H. A. Abdul-Rashid · R. Penny · M. Moghavvemi · S. W. Harun · H. Ahmad · W. S. Mohammed

Received: 8 July 2014 / Accepted: 13 October 2014 / Published online: 25 October 2014

Abstract This paper describes an analytical model developed to study the Fano resonance effect in clusters of spherical plasmonic nanoparticles under local excitation. The model depicted the case of a parallel single dipole emitter that was near-field coupled to a pentamer or heptamer cluster of nanospheres. Spatial polarization and field distributions of the optical states and resonance spectra for these cluster configurations were calculated. It was discovered that polarization interference between the nanoparticles triggered the formation of a second peak in the directivity spectra at 690 nm, and this in turn provided a mechanism for the occurrence of subradiant mode effects. The directivity calculation was analyzed in order to qualify the redirection of emission. Performances of various nanoantennae were investigated and fully characterized in terms of spatial geometric differences and the Fano resonance effect on plasmonic nanoparticles in the optical domain. Light radiation patterns were found to be significantly affected by nanosphere sizes and positioning of nanospheres with respect to the dipole. The analytical treatment of these modeled nanoantennae yielded results that are applicable to physical design and utilization considerations for pentamer and heptamer clusters in nanoantennae mechanisms.

S. D. Emami (✉) · M. R. K. Soltanian · A. Attaran · R. Penny · H. Ahmad
Photonic Research Center, University of Malaya, 50603 Kuala Lumpur, Malaysia
e-mail: s.d.emami@gmail.com

S. D. Emami · H. A. Abdul-Rashid
Faculty of Engineering, Multimedia University, 63100, Cyberjaya, Selangor, Malaysia

A. Attaran · M. Moghavvemi · S. W. Harun
Department of Electrical Engineering, Faculty of Engineering, University of Malaya, 50603 Kuala Lumpur, Malaysia

W. S. Mohammed
School of Engineering, Bangkok University, Klong Luang, Pathumthani 12120, Thailand

1 Introduction

The Fano resonance effect on plasmonic nanoparticle materials results in such materials possessing a number of unique optical properties, and the potential applicability for sensing [1], lasing [2], switching [3], nonlinear devices [4], and slow-light devices [5–7] has generated significant attention. A Fano resonance is a consequence of coherent interference between superradiant and subradiant hybridized plasmon modes [8]. Incident light on subradiant modes will initiate excitation that results in superradiant modes, and these superradiant modes possess zero or finite dipole moments alongside a comparably negligible coupling with light. The superradiant mode is strongly lifetime-broadened with a decay rate $\Gamma_{\text{Superradiant}}$ dependent on radiative and nonradiative losses, whereas the subradiant mode is weakly lifetime-broadened and has a decay rate of $\Gamma_{\text{Subradiant}} \ll \Gamma_{\text{Superradiant}}$, caused by nonradiative losses [9, 10]. This difference in decay rates allows for a significantly broadened spectral feature in superradiant modes in comparison with subradiant modes, mirroring the electromagnetic-induced transparency (EIT) phenomenon that is omnipresent in atomic systems [11, 12].

Fano resonance has been recently observed in a variety of complex plasmonic nanostructures, such as nanoshells [13], nanodisks [14], nanocubes [15], nanoparticle chains [16], carbon nanotubes [4], and nanoclusters [9, 10]. Research on nanoclusters has shown that the Fano resonance wavelength and amplitude spectrum are strongly

dependent on the dimensions, geometry, and relative size of the individual nanocluster and the dielectric environment [17]. Such findings allow for the Fano resonance effect to be optimally enhanced, and a maximum local density of optical states (LDOS) can be achieved by sufficiently increasing the overlap of the radiation pattern between subradiant and superradiant modes. LDOS affects practically all features of optical antennae, including excitation and emission rates [18]. Experimental observations of nanoclusters [18] allow for the Fano resonance superradiant mode to be considered as a promising candidate to enhance LDOS effects in nanoantennae.

None of the published investigations of the Fano resonance effect in nanoantennae have paid significant attention to the associated E-field distributions, directivity optimization, or bandwidth enhancement. This paper details the derivation of an electrodynamics coupling model for the interaction of dipolar transitions and radiation via plasmonic nanoclusters, such as quadrimers [19], pentamers [20, 21], and heptamers [18, 22]. The quantitative evolution of antennae modes, particularly the gradual emergence of subradiant and superradiant as antennae become increasingly bounded, is discussed. Geometrical properties of nanostructure antennae, such as sphere radius, inter-sphere distance, and distance of the cluster from the dipole, were evaluated over an appropriate range for the purpose of optimizing the directivity and bandwidth of the model. This analytical model was simulated using MATLAB commercial software and was validated using the finite integration technique (FIT) of the CST studio suite commercial product. The numerical simulations and analytical results described within this work were sufficient to allow determination of the optimum transmission directivity, intensity, and polarization using the basis of optimized nanosphere radius, inter-sphere distance, and distance between emitter and cluster.

2 Electrodynamics coupling model for nanoantennae

An electrodynamics coupling model was utilized for calculation of the scattered dipole field matrix (reflection and transmission) in the vicinity of nanoclusters. The analyzed configuration consisted of arrays of metallic nanospheres that were irradiated by an E-field emerging from a single dipole emitter. This emitter possessed a dipole moment with magnitude $\mathbf{P_0}$ located at the origin and along the *X*-axis. The induced dipole moment was described by Mei theory [23] as

$$\mathbf{P}_0 = \alpha_{ee}.\mathbf{E}_{exc}(\mathbf{r}_0.\mathbf{k}_B) \tag{1}$$

where α_{ee} is the electric polarizability of the nanoparticle, $\mathbf{r}_0$ and $\mathbf{k}_B$ are the distance from the emitter and background wave vectors, respectively, and $\mathbf{E}_{exc}$ is the exciting E-field produced cumulatively by the nanoparticles and any externally induced fields. The electric polarizability (α_{ee}) of a generic isolated particle may be expressed in terms of its Mie scattering coefficient c_1^{TM} (corresponding to a_n in the notation used in [24]). Such an expression arises by comparing the Mie TM^r spherical harmonic for $n = 1$ with the dipolar field generated by

$$\alpha_{ee} = -\mathbf{i}\frac{6\pi\varepsilon_0}{\mathbf{k}_B^3}a_1 \tag{2}$$

in which wavevector $\mathbf{K}_B = k_x\hat{\mathbf{X}} + k_y\hat{\mathbf{Y}} + k_z\hat{\mathbf{Z}}$ has amplitude $|\mathbf{K}_B| = (\omega/c)\sqrt{\varepsilon_B}$ for the exterior medium, where ε_B is the relative dielectric constant and c is the speed of light. Excitation by a periodic field results in each nanosphere forming an electric dipole moment of $\mathbf{P}_n = \mathbf{P}_0 e^{i\mathbf{k}_B.d_n}$, where $d_n = d_x\hat{\mathbf{X}} + d_y\hat{\mathbf{Y}} + d_z\hat{\mathbf{Z}}$ and n represents the index of nanoparticle positions [23].

Consideration of the model geometry allowed for the dipole moments (represented in plane waveform) to be expanded into spherical harmonics, which facilitated a solution for the scattered light. The expansion permitted the electric field produced by an electric dipole moment $\boldsymbol{p}_j$, to be expressed as [25]

$$\mathbf{E}_{scat}(\mathbf{r}) = \frac{e^{i\mathbf{k}_B r}}{4\pi\varepsilon_b\varepsilon_0 r^3}\{\mathbf{k}_B^2 r^2(\hat{\mathbf{r}}\times\hat{\mathbf{p}}_0)\times\hat{\mathbf{r}} + (1 - i\mathbf{k}_B r)[3(\hat{\mathbf{r}}\cdot\hat{\mathbf{p}}_0)\hat{\mathbf{r}} - \hat{\mathbf{p}}_0]\} \tag{3}$$

where $\mathrm{k_B}$ is wave vector and $\hat{\mathbf{p}}_0$ is induced dipole moment. For an incident field polarized in the $\hat{\boldsymbol{z}}$ direction, the excitation field $\mathrm{E}_{exc,j}$ at the center of a sphere j also lies along the $\hat{\boldsymbol{z}}$ direction. $\mathrm{E}_{exc,j}$ is the sum of the incident field and the field scattered by the other spheres and is represented in Eq. (4) wherein the unit vector $\hat{\mathbf{r}}$ points from sphere j to sphere l [26]:

$$\mathrm{E}_{exc,j} = \mathrm{E}_{inc,j} + \sum_{1\neq j}\gamma_{j,1}\tilde{\alpha_1}(\omega)\mathrm{E}_{exc,1} \tag{4}$$

in which $\gamma_{j,l} \equiv -e^{i\mathrm{k_b}R_{j,l}}\left(\frac{a_l}{R_{j,l}}\right)^3(1 - i\mathbf{k}_B R_{j,l} - \mathbf{k}_B^2 R_{j,l}^2)$

and where the dimensionless field coupling factors $R_{n,l} = |\mathbf{R}_{n,l}| = |\mathbf{r}_n - \mathbf{r}_l|$ are distance between different particle centers, and $R_{n,e} = |\mathbf{R}_{n,e}| = |\mathbf{r}_n - \mathbf{r}_e|$ represents distance of particles from the emitter in the Cartesian plane. The factor $\tilde{\alpha_n}(\omega)$ is the dimensionless polarizability function that can be simplified to:

$$\tilde{\alpha_n}(\omega) = \frac{\alpha_n(\omega)}{4\pi R_n^3} \tag{5}$$

where R_n is the radius of the nth sphere and α_n (ω) is particle polarizability as defined in [27]. Figure 1 illustrates the pentamer model structure as single-layered and located

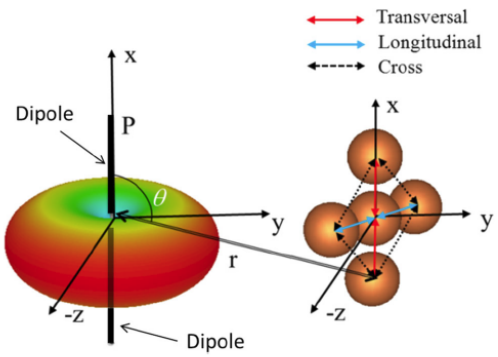

Fig. 1 Spatial schematic for a pentamer influenced by a dipole along the *X*-axis

perpendicular to the YZ plane at a distance of $x = R_{0,e} = \left|\mathbf{R}_{0,e}\right| = |\mathbf{r}_0 - \mathbf{r}_e|$ from the dipole. The response of each particle to the local incident electric field invoked a dipole moment $\boldsymbol{p}(\omega) = \varepsilon_0\varepsilon_b(\omega)\alpha_n \mathrm{E}_{\mathrm{exc}}(\omega)$, and $\varepsilon_b\ (\omega)$ is dielectric response of metal. The dielectric response $\varepsilon_b\ (\omega)$ was calculated using the Drude fit D + 2CP model for gold metal as shown in Eq. (6) [28]:

$$\varepsilon_b(\omega) = \varepsilon_\infty - \frac{\omega_{\mathrm{B}}^2}{\omega(\omega + i\delta)} + \sum_{p=1}^{2} A_p \Omega_P \left(\frac{e^{i\phi p}}{\Omega_P - \omega - i\Gamma_p} + \frac{e^{-i\phi p}}{\Omega_P + \omega + i\Gamma_p} \right) \tag{6}$$

where $\varepsilon_\infty = 1.1431$ is the dielectric response of background material, $\omega_B = 1.32 \times 10^{16}(\mathrm{rad\ s^{-1}})$ represents the bulk plasmon energy, $\delta = 1.805 \times 10^{14}(\mathrm{rad\ s^{-1}})$ is the damping ratio, and constants $A_1 = 0.26698$, $A_2 = 3.0834$, $\phi_1 = -1.2371$, $\phi_2 = -1.0968$ $\Omega_1 = 3.87 \times 10^{15}$, and $\Omega_2 = 4.16 \times 10^{15}$. In this model, the field strength of an arbitrary $\hat{z}$-polarized incident field at each particle position (as shown in Fig. 1) and the excitation fields was described as $\mathbf{E}_{\mathrm{ecx},n} = \mathrm{E}_{\mathrm{ecx},n}.\hat{\mathbf{r}}$, which represented the local excitation field created by external sources and all other particles.

Derivation of the dimensionless coupling coefficient between the particles and dipole and particles using Mei theory in Eq. (7) was necessary to calculate the coupling between particles and the coupling between the dipole and particles. This derivation process involved a dimensionless coefficient a_n expressed by the Riccati–Bessel function as follows [29–31]:

$$a_n = \frac{\psi_n(x)\psi_n'(mx) - m\psi_n'(x)\psi_n(mx)}{\xi_n(x)\psi_n'(mx) - m\xi_n'\psi_n(mx)} \tag{7}$$

where $\psi_n(x) = xj_n(x), \chi_n(x) = xy_n(x)$, and $\xi_n(x) = xh_n^{(1)}(x)$ are Riccati–Bessel, Riccati–Neumann, and Riccati–Hankel functions, respectively, $x = \mathbf{k}_{\mathrm{B}}R_{n,e}$, and the prime symbol $'$ denotes derivation with respect to the argument. Couplings between a nanoparticle and dipole, and between nanoparticles, were expressed after consideration of particle polarizability Eq. (2) in conjunction with introduced dimensionless field coupling factors $\gamma_{j,l}$ and $\gamma_{j,e}$. These latter factors represented the coupling between particles l and j, and between the emitter and a particle j, respectively. Based on the positions of the nanospheres and consideration of Eq. (4), the transverse, longitudinal, and cross-sectional coupling factors were described as follows [26].

For the transverse case where $\hat{\mathbf{r}}_1 \cdot \mathbf{p} = 0$ and $(\hat{\mathbf{r}}_l \times \mathbf{p}) \times \hat{\mathbf{r}}_l = \mathbf{p}$, the coupling factor was determined as:

$$\gamma_{j,l,T} \equiv -e^{i\mathbf{k}_b R_{j,l}} \left(\frac{a_l}{R_{j,l}}\right)^3 \left(1 - i\mathbf{k}_{\mathrm{B}}R_{j,l} - \mathbf{k}_{\mathrm{B}}^2 R_{j,l}^2\right) \tag{8}$$

$$\gamma_{j,e,T} \equiv -e^{i\mathbf{k}_b R_{j,e}} \left(\frac{a_j}{R_{j,e}}\right)^3 \left(1 - i\mathbf{k}_{\mathrm{B}}R_{j,e} - \mathbf{k}_{\mathrm{B}}^2 R_{j,e}^2\right) \tag{9}$$

For the longitudinal case where $\hat{\mathbf{r}}_1 \cdot \mathbf{p} = p$ and $(\hat{\mathbf{r}}_l \times \mathbf{p}) \times \hat{\mathbf{r}}_l = 0$, the coupling factors were:

$$\gamma_{j,l,L} \equiv -2e^{i\mathbf{k}_{\mathrm{B}}R_{j,l}} \left(\frac{a_l}{R_{j,l}}\right)^3 \left(i\mathbf{k}_{\mathrm{B}}R_{j,l} - 1\right) \tag{10}$$

$$\gamma_{j,e,L} \equiv -2e^{i\mathbf{k}_{\mathrm{B}}R_{j,e}} \left(\frac{a_j}{R_{j,e}}\right)^3 \left(i\mathbf{k}_{\mathrm{B}}R_{j,e} - 1\right) \tag{11}$$

For the cross-sectional case where $\hat{\mathbf{r}}_1 \cdot \mathbf{p} = \cos\theta$ and $(\hat{\mathbf{r}}_l \times \mathbf{p}) \times \hat{\mathbf{r}}_l = -\cos\theta$, the coupling factors were derived as:

$$\gamma_{j,l,C} \equiv -e^{i\mathbf{k}_{\mathrm{B}}R_{j,l}} \left(\frac{a_l}{R_{j,l}}\right)^3 \left(1 - i\mathbf{k}_{\mathrm{B}}R_{j,l} - \mathbf{k}_{\mathrm{B}}^2 R_{j,l}^2\right) \cos\theta \tag{12}$$

$$\gamma_{j,e,C} \equiv -e^{i\mathbf{k}_{\mathrm{B}}R_{j,e}} \left(\frac{a_j}{R_{j,e}}\right)^3 \left(1 - i\mathbf{k}_{\mathrm{B}}R_{j,e} - \mathbf{k}_{\mathrm{B}}^2 R_{j,e}^2\right) \cos\theta \tag{13}$$

Examination of Eqs. (8) to (13) revealed that the coupling coefficient factors were strongly proportional to the inverse cubic distance between two particles. Furthermore, the form of these coupled equations indicated that the dipole moment formula $\mathbf{p}(\omega) = \varepsilon_0\varepsilon_b\alpha(\omega)\mathbf{E}_{\mathrm{exc}}(\omega)$ could be solved using matrix inversion. The developed model described in this paper was able to provide moment derivations for quadrumer, pentamer, hexamer, and heptamer clusters with fully electrodynamically coupled dipoles [18].

3 Fano resonance model in optical nanoantennae

A Fano resonance plasmonic system can be described by the three-level quantum system [32] depicted in Fig. 2. The |1>, |2>, and |3> levels represent the incident photon at the ground, subradiant, and superradiant mode levels,

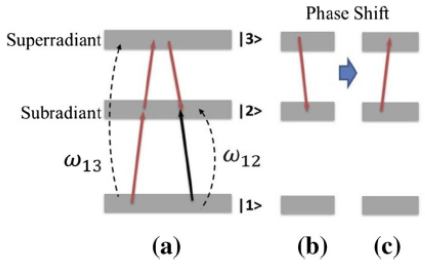

Fig. 2 Fano resonance in a three-level quantum system

respectively [11, 33]. A system pumped at superradiant wavelengths causes the superradiant mode to be engaged via two pathways, these pathways being |1> → |2> as indicated by the black arrow and |1> → |2> → |3> → |2> as depicted by the red arrow in Fig. 2a. Figure 2b illustrates the coupling among subradiant and superradiant modes that occurs between levels |2> and |3>, and this coupling contributes to phase shifting across a 0 to π range. The coupling mechanism invokes a delay between the incidence of the external electric field and the response of the plasmonic nanostructures, and this delay manifests as a phase shift. As ω increases, the phase increases from 0 at values below the resonance wavelength to $\pi/2$ at the resonance wavelength and to π as the resonance wavelength increases to infinity. Consequently, plasmonic nanostructures and the external electric field that were in phase before the resonance become out of phase after the resonance [34]. The Fano resonance effect appears when the combined phase shift from |2> → |3> and |3> → |2> is equal to π, since in this situation, the two paths cancel the polarization of the superradiant mode. This phenomenon results in a narrow window of transparency in the transmission spectrum [33].

Calculations related to the coupling matrix elements were simplified by using values obtained from the observed results of the E-field distribution [20, 21]. Figure 3a, d illustrates the E-field distribution in superradiant mode for a pentamer and a heptamer, respectively. Figure 3b, c provides a comparison of E-field distribution results for a pentamer with the Fano resonance peak at vertical and horizontal polarized angles. Figure 3e, f depicts vertical and 45° induced Fano resonance peak E-field from a dipole source in a heptamer cluster, respectively. Consideration of external E-field distributions for pentamer and heptamer clusters led to a hypothesis that the superradiant and subradiant modes, among all antennae radiant modes, were sufficient to explain all observations within the wavelength range of 400–1,000 nm [35]. The E-field distribution between nanospheres at superradiant and subradiant modes wavelength in pentamers and heptamers resulted in an absence of interactions between nanospheres in the outer ring of the cluster structure. Such behavior was due to the coupling factor (γ) between particles j and l (Eqs. (8) to (13)) being inversely proportional to the cube of the distance between two particles. In the case of E-field distribution at the Fano resonance wavelength, the couplings among nanospheres in all E-field polarizations cause excitation in those nanospheres along the E-field that cross the center out of the rest spheres, having similar interaction with the central nanosphere so that the effects of the other nanospheres on the generation of subradiant mode can be ignored.

Consideration of the E-field distribution observed results and stated hypotheses allowed for a simplification of the dipole analogy of the coupling matrix elements for the superradiant and subradiant modes, and this simplified calculation resulted in Eqs. (14) and (15), respectively:

$$\begin{bmatrix} \tilde{p}_1 \\ \vdots \\ \tilde{p}_N \end{bmatrix} = \begin{bmatrix} \tilde{\alpha}_1^{-1} & 0 & \cdots & 0 \\ 0 & \tilde{\alpha}_2^{-1} & \cdots & 0 \\ \vdots & \vdots & \ddots & \vdots \\ 0 & 0 & \cdots & \tilde{\alpha}_N^{-1} \end{bmatrix}^{-1} \begin{bmatrix} \mathrm{E}_{\mathrm{inc},1} \\ \\ \vdots \\ \mathrm{E}_{\mathrm{inc},N} \end{bmatrix} \tag{14}$$

$$\begin{bmatrix} \tilde{p}_1 \\ \vdots \\ \tilde{p}_N \end{bmatrix} = \begin{bmatrix} 0 & -\gamma_{1,2,X} & \cdots & -\gamma_{1,N,X} \\ -\gamma_{2,1,X} & 0 & \cdots & -\gamma_{2,N,X} \\ \vdots & \vdots & \ddots & \vdots \\ -\gamma_{N,1,X} & -\gamma_{N,2,X} & \cdots & 0 \end{bmatrix}^{-1} \begin{bmatrix} \mathrm{E}_{\mathrm{inc},1} \\ \\ \vdots \\ \mathrm{E}_{\mathrm{inc},N} \end{bmatrix} \tag{15}$$

where the notation X refers to the case of T (transverse), L (longitudinal), or C (cross-sectional). The matrix inversion in Eq. (14) is the dipole analog of the multi-pole T-matrix and incorporates both subradiant and superradiant modes. $\mathbf{E}_{\mathrm{inc}}$ is the incident field that interacts with each particle, while N represents the number of particles in both the pentamer and heptamer models. The interaction matrix has an inverse of α on the diagonal, while the off-diagonal elements describe the interaction between dipoles as determined by the electrodynamics coupling factor γ. For any dipole assembly, α can be inverted to find the polarization state $\tilde{p}$ induced by any interacting $\mathbf{E}_{\mathrm{inc}}$.

Superposition of the superradiant and subradiant modes (Eqs. (14) and (15)) resulted in coupled linear equations that can be written as:

$$\begin{bmatrix} \tilde{p}_1 \\ \vdots \\ \tilde{p}_N \end{bmatrix} = \begin{bmatrix} \tilde{\alpha}_1^{-1} & -\gamma_{1,2,X} & \cdots & -\gamma_{1,N,X} \\ -\gamma_{2,1} & \tilde{\alpha}_2^{-1} & \cdots & -\gamma_{2,N,X} \\ \vdots & \vdots & \ddots & \vdots \\ -\gamma_{N,1,X} & -\gamma_{N,2,X} & \cdots & \tilde{\alpha}_N^{-1} \end{bmatrix}^{-1} \begin{bmatrix} \mathrm{E}_{\mathrm{inc},1} \\ \\ \vdots \\ \mathrm{E}_{\mathrm{inc},N} \end{bmatrix} \tag{16}$$

3.1 Transmission and reflection analysis

The origin and polarization-independent nature of Fano resonance have been previously reported [36], in which the authors provided formal and rigorous definitions of the

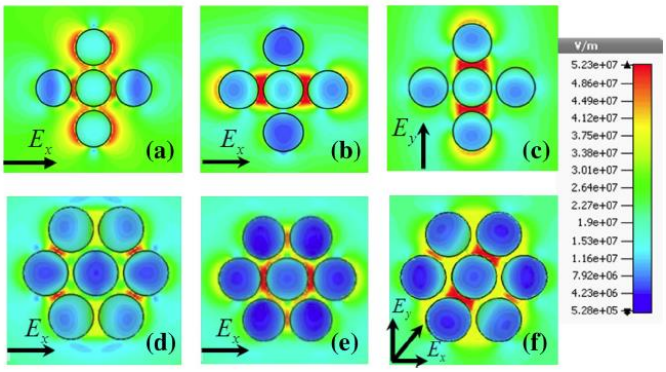

Fig. 3 External E-field distribution at Fano resonance wavelength. **a** E-field located along *X*-axis and the cluster plane located in XZ plane at 560 nm (superradiant mode) for pentamer. **b** E-field located along *X*-axis and the cluster plane located in XZ plane at 600 nm (Fano dip) for pentamer. **c** E-field located along *Y*-axis and the cluster plane located in XY plane at 600 nm (Fano dip) for pentamer. **d** E-field located along *X*-axis and the cluster plane located in XZ plane at 560 nm (superradiant mode) for heptamer. **e** E-field located along *X*-axis and the cluster plane located in XZ plane at 600 nm (Fano dip) for heptamer. **f** E-field located along 45° and the cluster plane located in XZ plane at 600 nm (Fano dip) for heptamer

distinct electric and magnetic eigenmodes present in their investigated systems. Verification of the Fano resonance model introduced here was aided by the transmission and reflection profiles of a dipole in the vicinity of pentamer and heptamer spectra being plotted in Fig. 4A.1, B.1, respectively. In analogy to nanoshell symmetry breaking [31], the signature of the subradiant mode became more apparent when the distance between two nanospheres in a pentamer or heptamer was reduced to 20–35 nm. The calculated subradiant mode reflection (Eq. (15)) and superradiant mode reflection (Eq. (14)) are demonstrated by the green dash-dotted and blue dotted line, respectively. The superposition of the calculated radiated field at the subradiant and superradiant modes (Eq. (16)) was responsible for the resulting transmission and reflection spectra. Reflection and transmission results of dipole radiation are shown by the red dashed line and solid black line, respectively, for which sphere radii was set at 70 nm. The existence of Fano resonance in a pentamer or heptamer also led to the formation of the subradiant mode, and this mode could be observed from reflection spectra in an asymmetric line shape at around 600 nm in Fig. 4A.1, B.1 for pentamer and heptamer, respectively. As detailed in the previous section, coupling between subradiant and superradiant modes contributed to phase shifting across a 0 to π range, and Fano resonance appeared when the combined phase shift was equal to π. Characteristics of the Fano resonances in the pentamer are explained by the examination of the electric field distributions at the respective spectral positions as shown in Fig. 4A.2, A.3. All of the nanoparticles oscillated in phase as a result of the charge distributions in the nanoparticles at the superradiant mode, as seen by reference to Fig. 4A.2. The E-field distribution pattern at the Fano resonance wavelength of 600 nm is plotted in Fig. 4A.3. Phase shifts of spheres 1, 3, and 5 with respect to spheres 2 and 4 led to the formation of the superradiant and subradiant modes [20]. As in the case with pentamers, heptamers having a superradiant mode experienced the oscillating plasmon in the seven nanoparticles as in-phase and exhibited significant mode broadening due to radiative damping. The trend of the transmission and reflection profiles in Fig. 4B.1 for the developed model agreed well with those of an earlier report [36].

In order to analyze the behavior of Fano resonance, the curves of phase change versus the E-field wavelength are shown in Fig. 4A.4 for quadrumers and pentamers, and in Fig. 4B.4 for hexamers and heptamers. For a quadrumer or hexamer, the phase shifting across a 0 to π range that contributed to the external electric field was—π phase before the resonance, and then 0 phase after the resonance [34]. As shown by red dashed line in Fig. 4A.4, B.4, a phase shift of π appeared at the Fano resonance wavelength when the subradiant and superradiant modes were invoked near the Fano resonance dip. This phenomenon was a consequence of the subradiant mode canceling the polarization of the superradiant mode and resulted in a narrow window of transparency in the transmission spectrum [33].

3.2 Analysis of optical directivity properties

Antennae are characterized by specific properties, such as directivity (D_{MAX}), spectral efficiency bandwidth, and radiation efficiency (ε_{rad}). The near-field coupling of quantum emitters to particle plasmon resonances provides

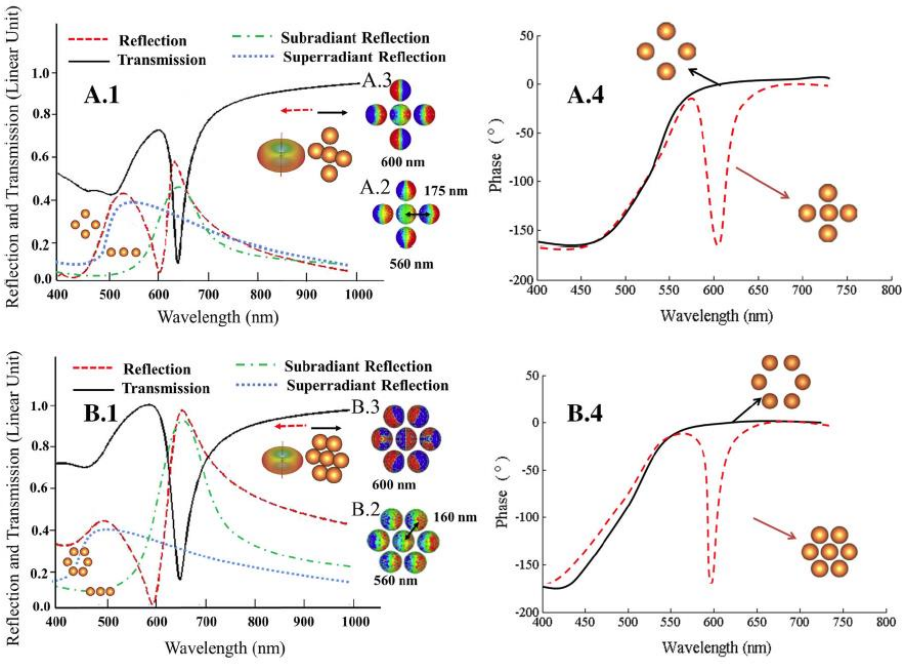

Fig. 4 **A.1** Reflection and transmission spectrum for a pentamer **A.2** E-field distribution pattern at 600 nm for a pentamer (Fano dip) **A.3** E-field distribution pattern at 560 nm (superradiant mode) for a pentamer **A.4** phase spectrum for a quadrumer and a pentamer **B.1** reflection and transmission spectrum for a heptamer **B.2** E-field distribution pattern at 600 nm for a heptamer (Fano dip) **B.3** E-field distribution pattern at 560 nm (superradiant mode) for a heptamer **B.4** Phase spectrum for a heptamer and an hexamer

a mechanism to redirect the light emission, while far-field radiation is completely determined by an antenna's mode [37, 38]. This redirection of emission is quantified by a directivity expression [37], while directivity properties of developed nanoantennae in the vicinity of subradiant and superradiant mode spectra were investigated in the current work. The assumption that the accumulation of all nanoparticle dipole moments within given spherical angles θ and φ can be referenced as $P(\theta, \varphi)$ permitted the simplified Eq. (17). The P_{rad} and P_{loss} factors are indicative of radiated and absorbed powers, respectively [39]. The maximum directivity of the antenna radiation (D_{MAX}) and radiation efficiency (η_{rad}) were given by:

$$D_{\text{MAX}} = \left(\frac{4\pi}{P_{\text{rad}}}\right)\text{MAX}[p(\theta,\varphi)] \quad \text{(a)}, \; \varepsilon_{\text{rad}} = \frac{P_{\text{rad}}}{P_{\text{rad}} + P_{\text{loss}}} \quad \text{(b)} \tag{17}$$

Figure 5a, b shows in 3D the directivity $D(\theta, \varphi)$ of a dipolar emitter in free space when coupled with a pentamer nanoantenna oriented along the y-axis. The dipole antenna acted solely as the feed element and was included for purposes of a reference situation. The 2D results in the two major planes for the dipolar emitter in free space are depicted in Fig. 5c, d. Dipole-coupled results in the vicinity of a pentamer nanoantenna are demonstrated in Fig. 5e, f. In this scenario, the emitter was placed 200 nm from the antenna element, while in contrast, the angular emission of the emitter coupled to the pentamer was strongly directed along the $+y$-axis. The maximum directivity of the emitter was 5.2, which about twice that of the dipole antenna maximum directivity.

3.3 Element optimization

3.3.1 Directivity analysis

Determining the optimum directivity of the subradiant mode in a pentamer nanoantenna required attention on three variables, these being nanoparticle radius, distance between the dipole resonator and nanoparticles, and gap between each nanoparticle in the model structure as shown in Fig. (6). The resonance wavelength was set at maximum directivity of the subradiant mode. Figure 6a illustrates the